

1 **TiO₂/Au/TiO₂ multilayer thin-film photoanodes synthesized**
2 **by pulsed laser deposition for photoelectrochemical**
3 **degradation of organic pollutants**

4 **Isidoro Olvera-Rodríguez^a, Rafael Hernández^a, Alejandro Medel^b, Carlos Guzmán^a,**
5 **Luis Escobar-Alarcón^c, Enric Brillas^d, Ignasi Sirés^{d,*}, Karen Esquivel^{a,**}**

6 *^a Posgrado de Ingeniería, Facultad de Ingeniería, Universidad Autónoma de Querétaro,*
7 *Cerro de las Campanas, C.P. 76000, Santiago de Querétaro, Qro., Mexico*

8 *^b Centro de Investigaciones y Desarrollo Tecnológico en Electroquímica, Parque Tecnológico*
9 *Querétaro s/n, Sanfandila, Pedro Escobedo, C.P. 76730, Qro., Mexico*

10 *^c Departamento de Física, Instituto Nacional de Investigaciones Nucleares, Carretera México*
11 *– Toluca s/n, La Marquesa Ocoyoacac, Mexico*

12 *^d Laboratori d'Electroquímica dels Materials i del Medi Ambient, Departament de Química*
13 *Física, Facultat de Química, Universitat de Barcelona, Martí i Franquès 1-11, 08028*
14 *Barcelona, Spain*

15 **Paper submitted to be published in *Separation and Purification Technology***

16 * Corresponding author: E-mail address: i.sires@ub.edu (I. Sirés)

17 Phone: +34 934039240. Fax: +34 934021231

18 ** Corresponding author: E-mail address: karen.esquivel@uaq.mx (K. Esquivel)

19 Phone: +52 (442)192 12 00. Fax: +52 (442) 192 13 25

20

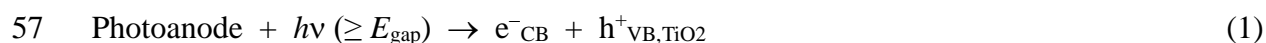
21 **Abstract**

22 Most commonly employed anodes for photoelectrochemical degradation of organic
23 contaminants in water are too thick, resulting in a lower degradation efficiency due to an
24 excessive electron-hole recombination. Multilayer-type TiO₂/Au/TiO₂ nanocomposites have
25 been prepared as photoanode thin films by pulsed laser deposition (PLD). The films were
26 composed of six TiO₂ and five Au alternate layers, with total thickness of about 212 nm,
27 aimed to optimize the absorption of photons and minimize the recombination. The influence
28 of gold on the optical, structural, and chemical properties of the semiconductor
29 nanocomposites was investigated. The band gap determined from Tauc model was 3.22 eV,
30 close to that obtained by spectroscopic ellipsometry and lower than that of the TiO₂ film,
31 revealing an enhancement of visible light absorption. The catalytic performance of PLD films
32 was evaluated by using them as anodes in electro-oxidation (EO) and photoanodes in
33 photoelectrocatalysis (PEC) to degrade 39-157 mg L⁻¹ paracetamol in sulfate medium. The
34 drug removal was very slow in EO, due to the low ability to form •OH on the anode surface,
35 which was significantly enhanced upon UVA irradiation in PEC. The presence of Cl⁻ allowed
36 a faster degradation by produced active chlorine. Finally, a hybrid process involving PEC +
37 photoelectro-Fenton (PEF) with an air-diffusion cathode yielded total paracetamol decay in 4-
38 5 min at an anodic potential of +4.0 V because of the efficient •OH generation from Fenton's
39 and photo-Fenton reactions. Hydroquinone, *p*-benzoquinone and hydroxylated products were
40 detected during EO and PEC. The generation of active chlorine was confirmed by identifying
41 a chlorinated derivative, *N*-(4-chloro-2-hydroxyphenyl)acetamide, in PEC + PEF treatment.

42 *Keywords:* TiO₂/Au/TiO₂ nanocomposites; Paracetamol; Photoanode; Photoelectrocatalysis;
43 Photoelectro-Fenton

44 1. Introduction

45 Photoelectrocatalysis (PEC) has emerged in recent years as a low cost electrochemical
46 advanced oxidation process (EAOP) for the efficient destruction of organic pollutants
47 contained in water. This method combines the action of mild photoirradiation and a small
48 anode potential (E_{bias} or E_{an}) or current (I_{appl}) allowing: (i) the promotion of electrons from the
49 valence band (VB) of the photoanode to its conduction band (CB), generating electron-hole
50 pairs on the catalyst surface (reaction (1)); (ii) the spatial separation of both charge carriers by
51 collection of the transferred electrons at the cathode, thus minimizing their recombination
52 with holes; and (iii) the generation of different reactive oxygen species (ROS) that can
53 degrade the organics, like $\text{O}_2^{\bullet-}$, HO_2^{\bullet} , H_2O_2 , O_3 and $\bullet\text{OH}$ [1,2]. Among them, hydroxyl
54 radicals ($\bullet\text{OH}$) have the pre-eminent oxidizing role due to their high redox potential ($E^0 = 2.8$
55 V|SHE), being mainly formed from water oxidation by holes (reaction (2)) [3] or anodic
56 oxidation at the photoanode (M) surface (reaction (3)) [4-7].



60 The performance of conventional PEC can be enhanced by employing a cathode with
61 great ability to electrogenerate H_2O_2 from two-electron O_2 reduction. This reaction is
62 especially efficient at carbonaceous substrates such as supported particles [8-11], fibers
63 [12,13], nanotubes [14,15], graphene [16,17], felts [18,19] or air-diffusion materials [20].
64 H_2O_2 can be reduced to $\bullet\text{OH}$ by e^-_{CB} via reaction (4) [21], although there is controversy about
65 the occurrence of such transformation [22]. Alternatively, H_2O_2 can be activated in other
66 EAOPs by metal catalysts like Fe^{2+} to yield $\bullet\text{OH}$ via Fenton's reaction (5), giving rise to the
67 electro-Fenton (EF) process [23,24]. The catalytic cycle can be sustained upon irradiation of

68 the solution with UVA light or sunlight in photoelectro-Fenton (PEF) and solar photoelectro-
69 Fenton (SPEF) systems, which allow the Fe^{3+} photoreduction to Fe^{2+} as well as the gradual
70 photodegradation of refractory metalorganic complexes [20,25]. It is worth to notice that few
71 works have investigated the coupling between PEC and EF [26,27] or PEF [21].



74 TiO_2 in its crystalline anatase phase is the most widely employed catalyst for
75 photoelectrochemical water decontamination, owing to its many virtues like non-toxicity, low
76 cost, excellent chemical and photochemical stability, and moderate band gap near the visible
77 range (3.2 eV, $\lambda = 387.5$ nm) [1]. In general, it is employed either as a nanostructure or a thin
78 film. In particular, there exist several deposition methods to grow high quality thin films. The
79 sol-gel synthesis is very common, but other techniques like particle assembly (e.g.,
80 electrophoresis), aqueous phase deposition (e.g., anodization, electrodeposition, and thermal
81 decomposition) and gas phase deposition (e.g., chemical vapor deposition, magnetron
82 sputtering, and spray coating) have also been investigated [28]. A less explored method is
83 pulsed laser deposition (PLD), which relies on substrate-coating by laser-induced plasma
84 [29]. Its advantages include flexibility, quick response, and congruent evaporation, yielding
85 highly crystalline and stoichiometric deposits [30].

86 The modification of TiO_2 with transition metals such as Cr, Co, or Fe allows extending
87 the TiO_2 absorption into the visible region but, in turn, they act as sites that stimulate the
88 electron-hole pair recombination and thermal instability [31]. Better performance of TiO_2 -
89 based heterostructures results from decoration with Cu [32-34] or noble metals like Ag
90 [35,36], Pd [37] and Au [38] due to their different Fermi level as compared to TiO_2 . Noble
91 metals act as an additional electron sink, facilitating the electron transfer from the
92 semiconductor CB to the metal particle. This improves the quantum yield because the

93 electron-hole recombination is reduced. Furthermore, these metals allow harnessing the
94 surface-plasmon resonance effect under visible light irradiation [39]. In the case of Au-TiO₂
95 nanocomposites, visible light at $\lambda = 560$ nm (close to the surface plasmon resonance [40])
96 may excite electrons from Au nanoparticles, to be further transferred to the CB of TiO₂.
97 Consequently, the accumulation of charge carriers is increased. In addition, as shown in
98 reaction (6), •OH may be formed on the Au surface upon oxidation of water [41]. The
99 potential occurrence of Au⁺ and Au³⁺ species also serves for the separation charge carriers [1].



101 Some authors have prepared Au-TiO₂ nanocomposite thin films as photoanodes by PLD
102 method, because of their precise and simultaneous control of stoichiometry, crystallinity and
103 thickness of the growing films upon accurate selection of the experimental process parameters
104 [42,43]. Several multilayer electrodes composed of Ni-Cu and Zn-Ni have been proven to
105 improve the mechanical and corrosive properties, reaching a higher catalytic activity with
106 longer service life as compared to simple alloys [44,45]. However, to the best of our
107 knowledge, the preparation of Au-TiO₂ multilayer electrodes and their application as
108 photoanodes for organic pollutants degradation has not been reported so far.

109 At present, many freshwater resources are seriously jeopardized by the presence of all
110 classes of pharmaceuticals used in human and veterinary medicine, which potentially entail
111 serious threats. The high relevance of this topic is confirmed from recent thematic surveys
112 conducted by world organizations like UNESCO [46], which have revealed the presence of
113 paracetamol (*N*-(4-hydroxyphenyl)acetamide) in the Baltic Sea. Worth highlighting,
114 paracetamol was the most prescribed drug in 2017 [47]. Several authors have treated
115 pharmaceuticals in aqueous media by PEC with TiO₂-based photoanodes [3,48-51], whereas
116 decoration with noble metals has been rarely addressed. For example, acetylsalicylic acid was
117 totally degraded by PEC with Pt-TiO₂ [52] and Pd-TiO₂ [53] under Xenon light illumination.

118 This work reports the synthesis of thin-film sandwich-type composites of TiO₂/Au/TiO₂
119 by PLD, aiming to enhance the photon adsorption and minimize the electron-hole pair
120 recombination upon PEC. The morphological, structural, and optical properties of synthesized
121 materials were analyzed by scanning electron microscopy (SEM), energy dispersive X-ray
122 spectroscopy (EDS), X-ray photoelectron spectroscopy (XPS), Raman spectroscopy, elastic
123 forward analysis (EFA), UV/Vis spectroscopy, photoluminescence, and spectroscopic
124 ellipsometry, whereas electrochemical characterization was made by cyclic voltammetry. The
125 PEC treatment of paracetamol solutions in sulfate medium in the absence and presence of
126 chloride ion was investigated for the best TiO₂/Au/TiO₂ film as photoanode. The hybrid
127 degradation by PEC + PEF was also examined.

128 **2. Experimental**

129 *2.1. Chemicals*

130 Paracetamol (99.9%) was of reagent grade purchased from Merck and used as received.
131 Sulfuric acid (used to adjust the pH), anhydrous sodium sulfate and sodium chloride
132 (background electrolytes) and Fe(II) sulfate heptahydrate (catalyst source for Fenton's
133 reaction) were of analytical grade purchased from Fluka and Panreac. All solutions were
134 prepared with pure water (Millipore Milli-Q system, resistivity >18.2 MΩ cm at room
135 temperature). Other chemicals were also of reagent or HPLC grade purchased from Sigma-
136 Aldrich, Probus and Panreac.

137 *2.2. Synthesis of thin-film photoanodes*

138 Different deposition conditions were employed in order to optimize the properties and
139 performance of the thin films obtained by PLD. Hereby, the optimum parameters are
140 described. Once the pressure, close to 8×10^{-6} Torr, was reached in the reaction chamber, the
141 deposition was performed. Multilayer thin films were deposited by alternating two laser

142 ablation plasmas produced using an Nd:YAG laser, with emission at the third harmonic ($\lambda =$
143 355 nm) and a pulse duration of 5 ns, working at a frequency of 10 Hz. For this purpose, the
144 laser beam was divided in two using a beam splitter. The obtained laser beams were focused
145 onto the targets with 50 cm focal length spherical lenses. High purity (99.99%) TiO₂ and gold
146 were used as targets. The laser fluence on both targets was constant, close to 4.0 J cm⁻². The
147 multilayer structure was obtained as follows: (i) the deposition started with only the TiO₂
148 ablation plasma acting for 5 min; (ii) afterwards, the laser beam on the TiO₂ target was
149 blocked using a mechanical shutter and the gold ablation plasma was produced for 30 s; (iii)
150 the laser beam on the Au target was then blocked and the ablation of the TiO₂ target was
151 initiated again. This procedure was repeated 5 times to attain a deposition time of 2.5 min for
152 Au. The film was deposited on a conductive glass substrate of 4.5 cm² surface area placed at
153 7 cm from the TiO₂ target surface.

154 *2.3. Procedures and characterization techniques*

155 The gold content in the films was determined by EDS using a microprobe attached to a
156 JEOL JSM 6510LV scanning electron microscope, with an acceleration voltage of 15 kV.
157 XPS was used to determine the chemical states of the elements in the films. The
158 measurements were performed in a PHI 5500 Multitechnique System from Physical
159 Electronics, with a monochromatic X-ray source (aluminum K α line of 1486.6 eV and 350
160 W) placed perpendicular to the analyzer axis and calibrated using the 3d_{5/2} line of Ag with a
161 full width at half maximum (FWHM) of 0.8 eV. The analyzed area was a circle of 0.8 mm
162 diameter, whereas the selected resolution for the spectra was 187.85 eV of Pass Energy (PE)
163 and 0.8 eV per step for the survey spectra and PE = 23.5 eV and 0.1 eV per step for the
164 narrow spectra of the different elements. All measurements were made in an ultra-high
165 vacuum (UHV) chamber at pressures between 5 $\times 10^{-9}$ and 2 $\times 10^{-8}$ Torr. The EFA
166 characterization was carried out using a 12.0 MeV C²⁺ ion beam from a Tandem Van de Graff

167 accelerator. The angle between the ion beam and the sample surface was set at 30° while the
168 angle between the detected particles and the incident ion beam was 45°. The microstructure
169 was studied by Raman spectroscopy, employing a micro-Raman LabRam 800 system
170 equipped with a confocal Olympus BX40 microscope and a 100X objective. The energy
171 source was an Nd:YAG laser at the second harmonic ($\lambda = 532$ nm) and the spectra were
172 calibrated with the monocrystalline Si line at 521 cm^{-1} .

173 Optical measurements were performed on a Perkin Elmer Lambda 35 UV/Vis
174 spectrophotometer to obtain the transmittance spectra of the films from 200 to 800 nm. A
175 FluoroMax 4 spectrofluorometer from Horiba Jobin Yvon was used to obtain the
176 photoluminescence (PL) spectra employing a 150 W Xenon lamp as excitation source.
177 Emission spectra were acquired from 365 to 650 nm, in order to avoid the first and second
178 order of the Rayleigh scattering, using 350 nm excitation wavelength.

179 The spectroscopic ellipsometry was performed in a M44 J.A Woollam rotating analyzer
180 ellipsometer, with an incidence angle of 70°. The ellipsometric parameters (amplitude psi, and
181 phase delta) were measured in the 1.62-4.40 eV photon energy range (763.2-281.5 nm). The
182 method used to analyze the results was effective medium approximation (EMA) model in
183 order to obtain the optical properties of the deposits.

184 The electrochemical characterization was performed by cyclic voltammetry with an
185 Autolab PGSTAT30 potentiostat. Up to 5 consecutive cycles were made at 100 mV s^{-1} within
186 the range from +3 V to -2 V vs. Ag|AgCl. An undivided electrochemical cell containing 50
187 mL of 0.050 M Na_2SO_4 at pH 3.0 thermostated at 25 °C was used. It was equipped with a
188 synthesized thin-film nanocomposite, a rolled platinum thread, and Ag|AgCl (3 M KCl)
189 electrode as the working, counter, and auxiliary electrodes, respectively. The exposed area of
190 the working electrode was 1 cm^2 . All potentials are referred to the reference electrode. Before
191 each run, O_2 was purged from the solution with gentle N_2 stream for 20 min, keeping it above

192 the solution during the analysis. Comparative cyclic voltammograms were made with pure
193 gold and undoped thin film as the anode to better characterize the behavior of the
194 TiO₂/Au/TiO₂ films.

195 The pH and electrical conductance of all solutions were measured with a Crison 2000
196 pH-meter and a Metrohm 644 conductometer, respectively. To assess the paracetamol
197 degradation, samples of 1.5 mL were withdrawn every 30 or 60 min, immediately diluted
198 with acetonitrile to stop the degradation and then, 50 µL aliquots were injected into a Waters
199 600 LC fitted with a C18 BDS Hypersil, 250 mm × 4.6 mm, column with particle size of 5
200 µm. Isocratic analyses were carried out using a 70:30 (v/v) acetonitrile/K₂HPO₄ mixture as
201 mobile phase at 0.8 mL min⁻¹. The retention time for paracetamol was 2.5 min, showing a
202 characteristic absorption peak at $\lambda = 243$ nm. All samples were microfiltered with 0.45 µm
203 Whatman PTFE filters. Experiments were run at least in duplicate and mean values from
204 HPLC analyses are reported.

205 GC-MS analysis of treated solutions was made with an Agilent Technologies system
206 composed of a 6890N gas chromatograph coupled to a 5975C mass spectrometer in EI mode
207 at 70 eV. A nonpolar Teknokroma Sapiens-X5ms and a polar HP INNOWax column, both of
208 0.25 µm, 30 m × 0.25 mm, were used. The temperature ramp was: 36 °C for 1 min, 5 °C min⁻¹
209 up to 320 °C, and hold time of 10 min. The temperatures of the inlet, source and transfer line
210 were 250, 230 and 300 °C, respectively. Liquid-liquid extractions were employed to obtain
211 the final samples to be injected. The mass spectra were analyzed with NIST05 MS database.

212 *2.4. Treatment of paracetamol solutions*

213 To evaluate the electroactivity and photoactivity of the synthesized thin films,
214 paracetamol was used as model pollutant. An open, undivided electrochemical cell,
215 thermostated at room temperature and containing 100 mL of solution, was employed. A
216 multilayer film anode was combined with a 316L stainless steel plate cathode, placed at a

217 distance of 2.5 cm and both with a geometric area of 4.3 cm². Paracetamol solutions (39-157
218 mg L⁻¹) in 0.050 M Na₂SO₄ or 0.035 M Na₂SO₄ + 0.015 M NaCl mixtures with the same
219 conductivity were treated at pH 3.0 and room temperature by electrochemical oxidation (EO,
220 without UVA radiation) and PEC using an Amel 2049 potentiostat-galvanostat, whereas the
221 potential difference between the anode and cathode (E_{cell}) was measured on a Demestres
222 601BR digital multimeter. These experiments were carried out in galvanostatic mode, and the
223 effect of the I_{appl} value was studied in PEC by running tests at 0.50, 1.00 and 1.50 mA (E_{an} of
224 1.7, 2.2 and 2.8 V vs. Ag|AgCl, and E_{cell} of 1.9, 2.7 and 3.3 V, respectively). From this study
225 and aiming to ensure the largest stability of the photoanode, 0.50 mA was selected as
226 optimum I_{appl} . In all cases, the solution was magnetically stirred at 800 rpm and the
227 experiments lasted 360 min. For the photo-assisted tests, a 36 W semicircular LED UVA
228 lamp surrounding the cell was used as the light source, and the entire setup was placed in a
229 purpose-made mirror box to favor the radiation collection through the solution. The UV
230 irradiance was 88 W m⁻², as measured on a radiometer.

231 In the PEC + PEF experiments, the stainless steel plate was replaced by a 3 cm² carbon-
232 polytetrafluoroethylene air-diffusion cathode supplied by Sainergy Fuel Cell, mounted as
233 described elsewhere and fed with air pumped at 1 L min⁻¹ for continuous H₂O₂ generation
234 [54,55]. A concentration of 0.50 mM Fe₂SO₄ was employed and the interelectrode gap was
235 about 1 cm. The applied E_{an} was +4.0 V vs. Ag|AgCl, yielding $E_{\text{cell}} = 4.6$ V. In all cases, the
236 solution pH was chosen as 3.0 since it is the optimum value for Fenton's reaction (5)
237 occurring in PEF.

238 3. Results and discussion

239 3.1. Characterization of thin films

240 The photoelectrochemical activity of TiO₂-based films depends on their morphological,
241 structural, optical, and electrical properties. In particular, it is crucial to keep the thickness of
242 the deposit as low as possible, being the thin films the most efficient alternatives. Thick
243 coatings lead to the presence of useless material, which cannot be photoactivated and, in
244 addition, increases the recombination.

245 Semi-transparent TiO₂/Au/TiO₂ thin films were obtained at the optimum deposition
246 conditions described in Section 2.1. According to SEM analysis (not shown), the surface was
247 smooth with some dispersed gold nanoparticles with diameter around 25 nm. The
248 corresponding EDS analysis allowed determining the composition of the thin film as 87.8
249 at.% oxygen, 11.8 at.% titanium, and 0.4 at.% gold.

250 The XPS spectrum of Fig. 1 evidences the presence of signals related to oxygen, titanium
251 and gold in the thin film. The other signals correspond to the substrate (Si 1s) and to
252 adventitious carbon. The signals at 460, 59 and 33 eV can be related to different orbital line
253 positions of titanium. The signal at 530 eV is ascribed to oxygen (O 1s), whereas that at 87 eV
254 belongs to gold (Au 4f). Fig. S1 in Supplementary Material shows the XPS spectrum of each
255 element. The Ti 2p region shown in Fig. S1-A reveals the presence of two signals: the first
256 one located at 457.9 eV and the second one at 463.5 eV, corresponding to the 2p_{3/2} and 2p_{1/2}
257 orbital levels, due to the spin orbital coupling effect, which can be attributed to Ti⁴⁺ [56-59],
258 with binding energy difference of 5.6 eV [60]. Note that a mathematical analysis of the Ti 2p
259 region showed that the Ti⁴⁺ and Ti³⁺ signals appeared in the same position, suggesting that
260 both oxidation states of the titanium are actually present in the composite. The XPS spectrum
261 of gold in Fig. S1-B presents two main signals, thus forming a doublet: one at 84.3 eV
262 corresponding to Au 4f_{7/2} core level and another peak at 89.4 eV corresponding to Au 4f_{5/2}.
263 The XPS spectrum of O 1s in Fig. S1-C suggests that the lattice of the material was modified.
264 This is inferred from the band located at about 530 eV, which is composed of three signals:

265 the first one at 529.0 eV attributed to the oxygen vacancies, the next peak at 530.7 eV due to
266 the ordering in the lattice of Ti-O-Ti (i.e., crystal lattice oxygen), and the last one at 531.9 eV
267 arising from the formation of hydroxyl groups on the TiO₂ surface [61]. The oxygen
268 vacancies were formed by the presence of gold in the structure [61,62]. The XPS spectrum of
269 C 1s in Fig. S1-D shows three signals: the band at 284.0 eV corresponds to the C-C bond, and
270 other one, at 287.8 eV, can be explained by the interaction between carbon and oxygen in the
271 surface [56,58,63].

272 The Raman spectrum shown in Fig. 2 displays vibrational modes at 139 cm⁻¹ (B_{1g}), 445
273 cm⁻¹ (E_g), 607 cm⁻¹ (A_{1g}), and 795 cm⁻¹ (B_{2g}) corresponding to the rutile crystalline phase of
274 TiO₂ [59,64]. A shift of the B_{1g} signal, from 145 to 139 cm⁻¹, is observed, suggesting
275 distortion of the TiO₂ lattice due to the presence of gold. The features of the Raman spectrum
276 indicate high crystallinity of the thin film. Furthermore, regarding the vibrational modes, the
277 lattice vibrations could be assigned as follows: (i) the B_{1g} mode corresponds to a symmetric
278 bending vibration of O-Ti-O, (ii) the E_g mode is due to a symmetric stretching vibration of O-
279 Ti-O, and (iii) the A_{1g} mode is attributed to an anti-symmetric bending vibration of O-Ti-O.
280 Considering the main vibrational modes E_g and A_{1g}, it is possible to determine the role of the
281 phonons in the excitation process of the lattice. The first one (E_g) is produced by acoustic
282 phonons that could contribute to the promotion of charge separation, whereas the second one
283 is caused by longitudinal optical phonons that promoted a higher recombination time and,
284 simultaneously, the generation of superoxide radicals since they are located in the conduction
285 band [65].

286 To gain better insight about gold distribution in the film, EFA analysis was carried out.
287 The general spectrum of Fig. 3A shows the signals of the elements present in the film, namely
288 O, Si, Ti and Au, in good agreement with the chemical composition determined by EDS. The
289 Si signal was due to the substrate. Fig. 3B shows the signal corresponding to Ti, revealing that

290 this element is distributed almost uniformly along the film thickness, with a slight increase in
291 the interface direction. Fig. 3C shows five well-defined peaks arising from the five gold layers
292 sandwiched by titania, thus forming the thin film structure
293 (TiO₂/Au/TiO₂/Au/TiO₂/Au/TiO₂/Au/TiO₂/Au/TiO₂) [66,67]. Note that equidistant peaks are
294 indicative of good control in the location of Au within the multilayer structure upon variation
295 of Ti deposition time. The Au signals increase from the inner to the outlet layer, in agreement
296 with the decrease of the Ti signal. Therefore, EFA results provide a clear evidence of the
297 multilayer structure formed.

298 The transmittance spectra of Fig. 4A show that the addition of gold in the film has two
299 important effects: it improves the light absorption and shifts the absorption edge to the visible
300 spectral region, which was one of the goals of this work. Another obvious feature in the
301 transmittance spectra is the presence of maxima and minima, which are due to interference
302 effects [68], from which the thickness and refractive index can be determined using the model
303 of Goodman [69]. The thickness values were 188 nm for the sample without gold and 212 nm
304 for the one containing gold. For the same samples, the refractive index was 2.4 and to 2.1,
305 respectively. In addition, the band gap was determined from the UV/Vis spectra using the
306 Tauc method assuming indirect transitions [70]. This was done by plotting $(\alpha h\nu)^2$ as a
307 function of the energy, as depicted in Fig. 4B. The optical absorption coefficient was obtained
308 as $\alpha = -\ln(T)/t$, where t is the film thickness and T the transmittance. Fig. 4B shows the linear
309 fits and the band gap value obtained for each film. Good fits to the experimental curves were
310 obtained for both samples. As can be seen, the band gap value obtained for the TiO₂ film was
311 3.48 eV, whereas a lower value, 3.22 eV, was obtained for the multilayer film [61]. The
312 higher band gap of undoped TiO₂ as compared to typical TiO₂ can be attributed to the
313 presence of oxygen vacancies, which act as barriers and hence, the whole composite behaves

314 as a kind of electrical insulator. Consequently, the photon effect over the surface causes a
315 shift of the band gap, requiring a higher energy to be activated.

316 Fig. 5A shows that the PL spectrum of the TiO₂ film consists of a broad emission band
317 from 2.0 to 3.3 eV, which can be mainly attributed to oxygen vacancies. The maximum of
318 emission found at 3.09 eV can be related to an interband transition. The high intensity of the
319 PL signal suggests a high recombination rate of the photogenerated charges in this sample.
320 When gold was incorporated in the film, a strong quenching of PL emission (Fig. 5A) as well
321 as a red shift (Fig. 5B) were observed. These results reveal that PL emission depends strongly
322 on the Au presence, promoting a decrease of the recombination rate. This result suggests a
323 more suitable photocatalytic response of the TiO₂/Au/TiO₂ multilayer thin film.

324 To confirm the results obtained by UV/Vis and PL spectroscopy, spectroscopic
325 ellipsometry analysis was carried out. To reproduce the parameters, a stratified model was
326 required, which could be simple as an interface or very complex. Based on the morphology of
327 the films, the properties of a mixture of two materials, Au and TiO₂, were simulated to
328 emulate an effective refractive index of the layer using the EMA model, which allows
329 approximating the optical properties of the whole thin film and addresses the individual
330 properties of the material and its volume fraction contribution. The model was adjusted until a
331 suitable agreement between the experimental values and the model of psi (Ψ) and delta (Δ)
332 fitted values vs the wavelength was obtained [71]. The good fit shown in Fig. S2 in
333 Supplementary Material allowed determining a roughness value of 13.75 ± 2.22 nm,
334 practically invariable in all the film. This is a good feature because it means that the surface
335 will be hard to mess up by the penetration of the dissolved pollutants when it will be used in
336 the photocatalytic tests.

337 The band gap value was alternatively obtained from ellipsometric measurements by
338 plotting the absorption coefficient vs energy. Since the Au/TiO₂/Au multilayer thin film

339 exhibited a certain thickness gradient, up to three different colored fringes (yellow, blue, and
340 purple) were observed on its surface. Hence, three curves were obtained, one for each zone in
341 the film, which were compared with a titanium blank, as can be seen in Fig. S3 in
342 Supplementary Material. In the three scanned zones, the band gap value showed almost no
343 variation and thus, it is possible to state that the excitation energy was not influenced by the
344 changing films thickness. Furthermore, it can be observed that the band gap changed when the
345 material was modified with gold, also changing the optical constant, which again confirms the
346 enhanced light absorption as a result of the presence of oxygen vacancies [42]. Worth noting,
347 the band gap values were near to those obtained from Tauc plots (Fig. 4B).

348 From EFA and ellipsometry spectroscopy, it is clear that gold was distributed with a
349 gradient over the surface. This does not imply a variation in the optical parameters along the
350 thin film, which remained constant, but it is evident that the gold incorporation in the titania
351 changed the optical response of the material, with dominance of the TiO₂ optical properties in
352 the thin film. This suggests that even performing the synthesis of independent layers, gold
353 mainly behave as a dopant that improved the optical performance of TiO₂.

354 *3.2. Electrochemical activity of thin films*

355 The electrochemical behavior of the synthesized multilayer thin film was studied by
356 cyclic voltammetry in 0.050 M Na₂SO₄ at pH 3.0. Fig. 6A and B present the cyclic
357 voltammograms recorded for pure Au and the unmodified TiO₂ film, respectively, under the
358 same conditions at a scan rate of 100 mV s⁻¹. Fig. 6A shows the expected *I-E* plot for pure Au
359 within the potential window from -0.80 to +1.25 V, with the oxidation peak of Au to Au₂O₃
360 close to +0.74 V and the corresponding reduction peak at +0.46 V, in agreement with
361 previous work [72]. In the case of TiO₂, Fig. 6B evidences a clear oxidation of water
362 originating adsorbed •OH within the potential range between +0.50 and -2.00 V [73]. On the
363 other hand, Fig. 6C depicts the profile obtained for the TiO₂/Au/TiO₂ multilayer anode, where

364 a shift to more positive values of the oxidation/reduction peaks potentials related to Au, as
365 well as the adsorption/desorption potentials for $\bullet\text{OH}$ corresponding to TiO_2 can be observed.
366 This can be attributed to superficial defects of the anode. These findings suggest that
367 pollutants could be oxidized more rapidly, thus enhancing the removal efficiency. Note that
368 the potential window for the multilayer film was narrowed as compared to that of the
369 unmodified one (see Fig. 6B and C), which may be an effect of the superficial defects
370 promoted by the gold incorporation in the lattice.

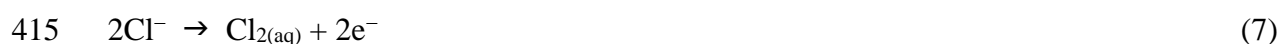
371 An electrochemical surface area of 0.9912 cm^2 with a roughness factor of 0.2305 was
372 estimated for the multilayer thin film using the desorption hydrogen zone between +0.02 and -
373 0.29 V. This area is close to the geometric one of 1 cm^2 considered for the cyclic voltammetry
374 experiments. Since the thickness of the film was very small, around 212 nm, one can infer
375 that the electrode surface possessed a low active site density.

376 *3.3. Paracetamol degradation by single and hybrid PEC processes*

377 The performance of the multilayer thin film as anode or photoanode was assessed from
378 the degradation of 100 mL of aqueous solutions of paracetamol at pH 3.0. Several preliminary
379 tests were made with 157 mg L^{-1} of the drug: (i) no change in its concentration was found by
380 direct irradiation of the solution with the 36-W LED UVA lamp, suggesting that paracetamol
381 was not photoactive under such conditions, (ii) a very small drug decay was obtained upon
382 irradiation of a $\text{TiO}_2/\text{Au}/\text{TiO}_2$ thin film of 4.3 cm^2 area immersed in the solution, evidencing
383 the accumulation of a low quantity of $\bullet\text{OH}$ from reactions (2) and (6) by photocatalysis, due
384 to the fast electron-hole recombination, and (iii) similar degradation performances were
385 measured by applying 0.50, 1.00, and 1.50 mA under PEC conditions and hence, to ensure the
386 highest stability and duration of the film, an $I_{\text{app}} = 0.50\text{ mA}$ was utilized in galvanostatic PEC
387 experiments.

388 Several assays were made to show the performance of PEC for paracetamol contents
389 between 39 and 157 mg L⁻¹ in sulfate matrices without or with Cl⁻. First, comparative EO
390 experiments were made in 0.050 M Na₂SO₄ and the results are presented in Fig. 7A. As can
391 be seen, a gradual normalized drug decay was always found until 300 min of treatment,
392 attaining a smaller reduction of 47%, 37%, and 29% as the drug content was increased. Since
393 at $I_{app} = 0.50$ mA the E_{an} was +1.7 V, higher than the potential value needed for water
394 oxidation to •OH via reaction (3), one can expect a certain production of this radical with
395 ability to attack the drug, in concomitance with its direct anodic oxidation. Note that, in these
396 trials, the total content of paracetamol degraded gradually rose. The quantity of available •OH
397 was enhanced due to the deceleration of the parasitic reactions of this radical, pre-eminently
398 its oxidation to O₂ [4,23,24]. The same reasons can justify the greater drug content removed,
399 although accounting for a lower percentage, at higher organic load upon PEC treatment in
400 0.050 M Na₂SO₄ (Fig. 7B). In this case, the large quantity of additional •OH formed from
401 reactions (2) and (6) under UVA light irradiation, resulting from the minimization of the
402 electron-pair recombination thanks to current supply, caused a faster degradation as compared
403 to EO. Thus, 95%, 69% and 61% drug disappeared at the end of the treatment of 39, 78 and
404 157 mg L⁻¹ paracetamol, respectively. The pollutant decayed much more rapidly in a mixed
405 sulfate + chloride matrix (Fig. 7C), yielding overall removal at 120 min for 39 mg L⁻¹ and at
406 150 min for 78 mg L⁻¹, but only attaining a 50% decay for 157 mg L⁻¹. The faster degradation
407 in the two former solutions can be ascribed to the quicker destruction of organics by active
408 chlorine species formed from oxidation of Cl⁻ to dissolved Cl₂ at the photoanode via reaction
409 (7), followed by hydrolysis to hypochlorous acid (HClO) via reaction (8) [74]. HClO is the
410 strongest active chlorine species and predominates over Cl₂ at pH 3.0, then competing with
411 •OH to attack the paracetamol molecules [8,23,24]. However, it is well known that •OH may
412 be scavenged by Cl⁻. The partial destruction of generated radicals could explain the strong

413 inhibition of drug decay in Fig. 7C at 157 mg L⁻¹, suggesting that the oxidation of
414 paracetamol at low concentrations is pre-eminently determined by •OH.



417 Finally, the performance of the hybrid PEC + PEF process to degrade 39 mg L⁻¹ of
418 paracetamol in the mixed matrix with 0.50 mM Fe²⁺ using an air-diffusion cathode for H₂O₂
419 production was assessed. Fig. 8 evidences a total drug removal after only 4-5 min of
420 treatment, a time much shorter than by single PEC (Fig. 7C). This result can be explained by
421 the fast destruction of the parent molecule with the high amounts of •OH formed from
422 Fenton's reaction (5) in the bulk, much superior to the action of the other oxidizing agents
423 formed at the photoanode. In PEF treatment of 157 mg L⁻¹ paracetamol in 0.050 M Na₂SO₄
424 with 1 mM Fe²⁺ at pH 3.0 using a similar Pt/air-diffusion cell and working at 300 mA (i.e.,
425 E_{cell} of 13.0 V), a time of 6 min was needed for the total abatement of the drug [75]. The PEC
426 + PEF treatment with the TiO₂/Au/TiO₂ photoanode showed a greater viability, not only by
427 the shorter time needed for paracetamol disappearance, but also by the use of a less expensive
428 anode and the smaller energy consumption. E_{cell} was as low as 4.6 V at $E_{\text{an}} = +4.0$ V (i.e.,
429 current of 2.00 mA), making the process more cost-effective.

430 GC-MS analysis of the 39 mg L⁻¹ paracetamol solution in 0.050 M Na₂SO₄ treated by EO
431 and PEC showed the formation of aromatic products such as hydroquinone, its oxidation
432 product *p*-benzoquinone and hydroxylated derivatives like tetrahydroxy-*p*-benzoquinone.
433 Hydroquinone can be produced from the attack of •OH on the C(1)-position of the benzenic
434 ring of paracetamol with loss of acetamide [75]. These products have also been reported for
435 the treatment of this drug by several EAOPs [75-77]. The GC-MS analysis of the treated
436 paracetamol solution in the mixed matrix by the hybrid PEC + PEF process also allowed the
437 detection of a chlorinated product, namely *N*-(4-chloro-2-hydroxyphenyl)acetamide, during

438 the first 30 min of electrolysis, whereupon chlorinated molecules were no longer found. The
439 existence of this chlorinated product confirms the production of active chlorine that attacks
440 the C(4)-position of the target molecule, along with its hydroxylation on C(2)-position.

441 **4. Conclusions**

442 A novel TiO₂/Au/TiO₂ multilayer thin-film photoanode was obtained by PLD process,
443 showing a better visible light absorption than TiO₂. According to the optical characterization
444 by UV/Vis spectroscopy, photoluminescence and ellipsometry, the improved photoactivity
445 was due to gold incorporation in the titania matrix. From the structural analysis, rutile was
446 found as main titania phase, whereas the chemical interaction studied by XPS agreed with the
447 presence of metallic gold and Ti³⁺ in the oxide structure. The thin film was employed as
448 anode and photoanode to remove paracetamol from aqueous solutions. The EO treatment of
449 39 mg L⁻¹ of the drug in sulfate medium yielded a low degradation rate, only reaching 47%
450 removal, whereas irradiation with UVA light under the same conditions enhanced the
451 concentration decay up to 95%. The required time was halved upon production of active
452 chlorine in the presence of chloride ion. Finally the hybrid PEC + PEF process exhibited an
453 excellent synergy, achieving the complete disappearance of paracetamol in only 5 min.
454 Hydroquinone, *p*-benzoquinone and hydroxylated products were detected during EO and PEC
455 using 0.050 M Na₂SO₄, whereas a chlorinated derivative was identified during PEC + PEF in
456 the mixed matrix, confirming the generation of active chlorine. The photoactivity of Au-
457 modified TiO₂ thin films within the visible range opens the door to their application in solar
458 PEC and SPEC + SPEF treatments of organic pollutants.

459 **Acknowledgments**

460 The authors gratefully acknowledge financial support from project CTQ2016-78616-R
461 (AEI/FEDER, EU) and project CB-240998 (CONACYT, Mexico). I. Olvera-Rodríguez
462 thanks CONACYT for his fellowship and K. Esquivel thanks funding from FOFI-UAQ-2018
463 project.

464 **References**

- 465 [1] H. Zhang, G. Chen, D.W. Bahnemann, Environmental Photo(electro)catalysis:
466 Fundamental Principles and Applied Catalysts; in C. Comninellis, G. Chen (eds.),
467 Electrochemistry for the Environment, Springer Science+Business Media, LLC, New
468 York, USA, 2010.
- 469 [2] D. Cao, Y. Wang, X. Zhao, Combination of photocatalytic and electrochemical
470 degradation of organic pollutants from water, *Curr. Opinion Green Sustain. Chem.* 6
471 (2017) 78-84.
- 472 [3] S. Garcia-Segura, E. Brillas, Applied photoelectrocatalysis on the degradation of
473 organic pollutants in wastewaters, *J. Photochem. Photobiol. C: Photochem. Rev.* 31
474 (2017) 1-35.
- 475 [4] M. Panizza, G. Cerisola, Direct and mediated anodic oxidation of organic pollutants,
476 *Chem. Rev.* 109 (2009) 6541-6569.
- 477 [5] X. Yu, X. Han, Z. Zhenhuan, J. Zhang, W. Guo, C. Pan, A. Li, H. Liu, Z. Lin,
478 Hierarchical TiO₂ nanowire/graphite fiber photoelectrocatalysis setup powered by a
479 wind-driven nanogenerator: a highly efficient photoelectrocatalytic device entirely
480 based on renewable energy, *Nano Energy* 11 (2015) 19-27.
- 481 [6] G. Avgouropoulos, D. Mantzavinos, P. Lianos, Photoelectrocatalytic vs. photocatalytic
482 degradation of organic water born pollutants, *Catalysts* 8 (2018) 455 (10 pages).

- 483 [7] A. Turolla, M. Bestetti, M. Antonelli, Optimization of heterogeneous
484 photoelectrocatalysis on nanotubular TiO₂ electrodes: reactor configuration and kinetic
485 modelling, *Chem. Eng. Sci.* 182 (2018) 171-179.
- 486 [8] A. Thiam, E. Brillas, F. Centellas, P.L. Cabot, I. Sirés, Electrochemical reactivity of
487 Ponceau 4R (food additive E124) in different electrolytes and batch cells, *Electrochim.*
488 *Acta* 173 (2015) 523-533.
- 489 [9] G. Coria, I. Sirés, E. Brillas, J.L. Nava, Influence of the anode material on the
490 degradation of naproxen by Fenton-based electrochemical processes, *Chem. Eng. J.* 304
491 (2016) 817-825.
- 492 [10] A. Galia, S. Lanzalaco, M.A. Sabatino, C. Dispenza, O. Scialdone, I. Sirés, Crosslinking
493 of poly(vinylpyrrolidone) activated by electrogenerated hydroxyl radicals: a first step
494 towards a simple and cheap synthetic route of nanogel vectors, *Electrochem. Commun.*
495 62 (2016) 64-68.
- 496 [11] A. Thiam, E. Brillas, J.A. Garrido, R.M. Rodríguez, I. Sirés, Routes for the
497 electrochemical degradation of the artificial food azo-colour Ponceau 4R by advanced
498 oxidation processes, *Appl. Catal. B: Environ.* 180 (2016) 227-236.
- 499 [12] H. Lan, W. He, A. Wang, R. Liu, H. Liu, J. Qu, C.P. Huang, An activated carbon fiber
500 cathode for the degradation of glyphosate in aqueous solutions by the electro-Fenton
501 mode: optimal operational conditions and the deposition of iron on cathode on electrode
502 reusability, *Water Res.* 105 (2016) 575-582.
- 503 [13] C. Trelu, N. Oturan, F.K. Keita, C. Fourdrin, Y. Pechaud, M.A. Oturan, Regeneration
504 of activated carbon fiber by the electro-Fenton process, *Environ. Sci. Technol.* 52
505 (2018) 7450-7457.

- 506 [14] H. Roth, Y. Gendel, P. Buzatu, O. David, M. Wessling, Tubular carbon nanotube-based
507 gas diffusion electrode removes persistent organic pollutants by a cyclic adsorption –
508 electro-Fenton process, *J. Hazard. Mater.* 307 (2016) 1-6.
- 509 [15] C. Ridruejo, F. Alcaide, G. Álvarez, E. Brillas, I. Sirés, On-Site H₂O₂ electrogeneration
510 at a CoS₂-based air-diffusion cathode for the electrochemical degradation of organic
511 pollutants, *J. Electroanal. Chem.* 808 (2018) 364-371.
- 512 [16] T.X.H. Le, M. Bechelany, S. Lacour, N. Oturan, M.A. Oturan, M. Cretin, High removal
513 efficiency of dye pollutants by electro-Fenton process using a graphene based cathode,
514 *Carbon* 94 (2015) 1003-1011.
- 515 [17] E. Mousset, Z. Wang, J. Hammaker, O. Lefebvre, Physico-chemical properties of
516 pristine graphene and its performance as electrode material for electro-Fenton treatment
517 of wastewater, *Electrochim. Acta* 214 (2016) 217-230.
- 518 [18] N. Barhoumi, L. Labiadh, M.A. Oturan, N. Oturan, A. Gadri, S. Ammar, E. Brillas,
519 Electrochemical mineralization of the antibiotic levofloxacin by electro-Fenton-pyrite
520 process, *Chemosphere* 141 (2015) 250-257.
- 521 [19] O. Ganzenko, N. Oturan, I. Sirés, D. Huguenot, E.D. van Hullebusch, G. Esposito, M.A.
522 Oturan, Fast and complete removal of the 5-fluorouracil drug from water by electro-
523 Fenton oxidation, *Environ. Chem. Lett.* 16 (2018) 281-286.
- 524 [20] J.R. Steter, E. Brillas, I. Sirés, Solar photoelectro-Fenton treatment of a mixture of
525 parabens spiked into secondary treated wastewater effluent at low input current, *Appl.*
526 *Catal. B: Environ.* 224 (2018) 410-418.
- 527 [21] L.C. Almeida, B.F. Silva, M.V.B. Zanoni, Photoelectrocatalytic/photoelectro-Fenton
528 coupling system using a nanostructured photoanode for the oxidation of a textile dye:
529 kinetics study and oxidation pathway, *Chemosphere* 136 (2015) 63-71.

- 530 [22] Y. Nosaka, A. Nosaka, Understanding hydroxyl radical ($\cdot\text{OH}$) generation processes in
531 photocatalysis, *ACS Energy Lett.* 1 (2016) 356-359.
- 532 [23] E. Brillas, I. Sirés, M.A. Oturan, Electro-Fenton process and related electrochemical
533 technologies based on Fenton's reaction chemistry, *Chem. Rev.* 109 (2009) 6570-6631.
- 534 [24] C.A. Martínez-Huitle, M.A. Rodrigo, I. Sirés, O. Scialdone, Single and coupled
535 electrochemical processes and reactors for the abatement of organic water pollutants: a
536 critical review, *Chem. Rev.* 115 (2015) 13362-13407.
- 537 [25] I. Sirés, E. Brillas, Remediation of water pollution caused by pharmaceutical residues
538 based on electrochemical separation and degradation technologies: a review. *Environ.*
539 *Int.* 40 (2012) 212-229.
- 540 [26] Y.B. Xie, X.Z. Li, Interactive oxidation of photoelectrocatalysis and electro-Fenton for
541 azo dye degradation using TiO_2 -Ti mesh and reticulated vitreous carbon electrodes,
542 *Mater. Chem. Phys.* 95 (2006) 39-50.
- 543 [27] L.C. Almeida, B.F. Silva, M.V.B. Zanoni, Combined photoelectrocatalytic/electro-
544 Fenton process using a Pt/ TiO_2 NTs photoanode for enhanced degradation of an azo dye:
545 a mechanistic study, *J. Electroanal. Chem.* 734 (2014) 43-52.
- 546 [28] H. Zhang, X. Li, G. Chen, Fabrication of Photoelectrode Materials; in C. Comninellis,
547 G. Chen (eds.), *Electrochemistry for the Environment*, Springer Science+Business
548 Media, LLC, New York, USA, 2010.
- 549 [29] K.M. Beck, T. Sasaki, N. Koshizaki, Characterization of nanocomposite materials
550 prepared via laser ablation of Pt/ TiO_2 Bi-combinant targets, *Chem. Phys. Lett.* 301
551 (1999) 336-342.
- 552 [30] S. Murugesan, P. Kuppusami, N. Parvathavarthini, E. Mohandas, Pulsed laser
553 deposition of anatase and rutile TiO_2 thin films, *Surface Coat. Technol.* 201 (2007)
554 7713-7719.

- 555 [31] M. Pelaez, N.T. Nolan, S.C. Pillai, M.K. Seery, P. Falaras, A.G. Kontos, P.S.M.
556 Dunlop, J.W.J. Hamilton, J.A. Byrne, K. O'Shea, M.H. Entezari, D.D. Dionysiou, A
557 review on the visible light active titanium dioxide photocatalysts for environmental
558 applications, *Appl. Catal. B: Environ.* 125 (2012) 331-349.
- 559 [32] H.C. Arredondo Valdez, G. García Jiménez, S. Gutiérrez Granados, C. Ponce de León,
560 Degradation of paracetamol by advance oxidation processes using modified reticulated
561 vitreous carbon electrodes with TiO₂ and CuO/TiO₂/Al₂O₃, *Chemosphere* 89 (2012)
562 1195-1201.
- 563 [33] Ö. Kerkez, Í. Boz, Photo[electro)catalytic activity of Cu²⁺-modified TiO₂ nanorod array
564 thin films under visible light irradiation, *J. Phys. Chem. Solids* 75 (2014) 611-618.
- 565 [34] Z. Hua, Z. Dai, X. Bai, Z. Ye, P. Wang, H. Gu, X. Huang, Copper nanoparticles
566 sensitized TiO₂ nanotube arrays electrode with enhanced photoelectrocatalytic activity
567 for diclofenac degradation, *Chem. Eng. J.*, 283 (2016) 514-523.
- 568 [35] H.M. Sung-Suh, J.R. Choi, H.J. Hah, S.M. Koo, Y.C. Bae, Comparison of Ag
569 deposition effects on the photocatalytic activity of nanoparticulate TiO₂ under visible
570 and UV light irradiation, *J. Photochem. Photobiol. A: Chem.* 163 (2004) 37-44.
- 571 [36] R.B. Domínguez-Espíndola, C. Bruguera-Casamada, S. Silva-Martínez, R.M. Araujo, E.
572 Brillas, I. Sirés, Photoelectrocatalytic inactivation of *Pseudomonas aeruginosa* using an
573 Ag-decorated TiO₂ photoanode, *Separ. Purif. Technol.* 208 (2019) 83-91.
- 574 [37] Z. Zhang, Y. Yu, P. Wang, Hierarchical top-porous/bottom-tubular TiO₂ nanostructures
575 decorated with Pd nanoparticles for efficient photoelectrocatalytic decomposition of
576 synergistic pollutants, *ACS Appl. Mater. Interfaces* 4 (2012) 990-996.
- 577 [38] A. Pandikumar, S. Murugesan, R. Ramaraj, Functionalized silicate sol-gel-supported
578 TiO₂-Au core-shell nanomaterials and their photoelectrocatalytic activity, *ACS Appl.*
579 *Mater. Interfaces* 2 (2010) 1912-1917.

- 580 [39] Wang, H.; You, T.; Shi, W.; Li, J.; Guo, L. Au/TiO₂/Au as a plasmonic coupling
581 photocatalyst. *J. Phys. Chem. C* 116 (2012) 6490-6494.
- 582 [40] A. Ayati, A. Ahmadpour, F.F. Bamoharram, B. Tanhaei, M. Mänttari, M. Sillanpää,
583 Review on catalytic applications of Au/TiO₂ nanoparticles in the removal of water
584 pollutant, *Chemosphere* 107 (2014) 163-174.
- 585 [41] K.H.W. Ho, A. Shang, F. Shi, T.W. Lo, P.H. Yeung, Y.S. Yu, X. Zhang, K.-L. Wong,
586 D.Y. Lei, Plasmonic Au/TiO₂-dumbbell-on-film nanocavities for high-efficiency hot-
587 carrier generation and extraction, *Adv. Funct. Mater.* (2018) 1800383.
- 588 [42] E. György, G. Sauthier, A. Figueras, A. Giannoudakos, M. Kompitsas, I.N. Mihailescu,
589 Growth of Au–TiO₂ nanocomposite thin films by a dual-laser, dual-target system, *J.*
590 *Appl. Phys.* 100 (2006) 114302.
- 591 [43] G. Sahu, K. Wang, S.W. Gordon, W. Zhou, M.A. Tarr, Core-shell Au–TiO₂
592 nanoarchitectures formed by pulsed laser deposition for enhanced efficiency in dye
593 sensitized solar cells, *RSC Adv.* 2 (2012) 3791-3800.
- 594 [44] A. Maizelis, Multilayer nickel–copper anode for direct glucose fuel cell, *J. Electrochem.*
595 *En. Conv. Stor.* 16 (2019) 041003.
- 596 [45] A. Maizelis, B. Bairachny, Voltammetric analysis of phase composition of Zn-Ni alloy
597 thin films electrodeposited from weak alkaline polyligand electrolyte, *J. Nano-Electron.*
598 *Phys.* 9 (2017) 05010.
- 599 [46] UNESCO, Emerging Pollutants in Water Series, Vol. 1, Pharmaceuticals in the Aquatic
600 Environment of the Baltic Sea Region – A Status Report; 2017.
- 601 [47] Becker’s Hospital Review; [https://www.beckershospitalreview.com/supply-chain/10-](https://www.beckershospitalreview.com/supply-chain/10-most-popular-prescription-drugs-for-2017.html)
602 [most-popular-prescription-drugs-for-2017.html](https://www.beckershospitalreview.com/supply-chain/10-most-popular-prescription-drugs-for-2017.html) (last access in 2017).

- 603 [48] E. Brillas, I. Sirés, Electrochemical removal of pharmaceuticals from water streams:
604 reactivity elucidation by mass spectrometry, *TrAC-Trend. Anal. Chem.* 70 (2015) 112-
605 121.
- 606 [49] L. Liu, R. Li, Y. Liu, J. Zhang, Simultaneous degradation of ofloxacin and recovery of
607 Cu(II) by photoelectrocatalysis with highly ordered TiO₂ nanotubes, *J. Hazard. Mater.*
608 308 (2016) 264-275.
- 609 [50] I. Tantis, L.G. Bousiakou, P. Lianos, H. Kalkan, A study of the photocatalytic and
610 photoelectrocatalytic degradation of diclofenac sodium using nanocrystalline TiO₂
611 films, *J. Mater. Environ. Sci.* 8 (2017) 1-6.
- 612 [51] P. Mazierski, A. Fiszka, P. Wilczewska, A. Białk-Bielińska, A. Zaleska-Medynska, E.
613 Siedlecka, Removal of 5-fluorouracil by solar-driven photoelectrocatalytic oxidation
614 using Ti/TiO₂(NT) photoelectrodes, *Water Res.* 157 (2019) 610-620.
- 615 [52] Y. Cui, Q. Meng, X. Deng, Q. Ma, H. Zhang, X. Cheng, X. Li, M. Xie, Q. Cheng,
616 Fabrication of platinum nano-crystallites decorated TiO₂ nano-tube array photoelectrode
617 and its enhanced photoelectrocatalytic performance for degradation of aspirin and
618 mechanism, *J. Ind. Eng. Chem.* 43 (2016) 177-184.
- 619 [53] D. Li, J. Jia, T. Zheng, X. Cheng, X. Yu, Construction and characterization of visible
620 light active Pd nano-crystallite decorated and C-N-S-co-doped TiO₂ nanosheet array
621 photoelectrode for enhanced photocatalytic degradation of acetylsalicylic acid, *Appl.*
622 *Catal. B: Environ.* 188 (2016) 259-271.
- 623 [54] R. Burgos-Castillo, M. Sillanpää, E. Brillas, I. Sirés, Removal of metals and phosphorus
624 recovery from urban anaerobically digested sludge by electro-Fenton treatment, *Sci.*
625 *Total Environ.* 644 (2018) 173-182.

- 626 [55] E. Bocos, E. Brillas, M.A. Sanromán, I. Sirés, Electrocoagulation: simply a phase
627 separation technology? The case of bronopol compared to its treatment by EAOPs,
628 Environ. Sci. Technol. 50 (2016) 7679-7686.
- 629 [56] Z. Jiang, W. Zhang, L. Jin, X. Yang, F. Xu, J. Zhu, W. Huang, Direct XPS evidence for
630 charge transfer from a reduced rutile TiO₂(110) surface to Au clusters, J. Phys. Chem. C
631 111 (2007) 12434-12439.
- 632 [57] Y. Wu, J. Zhang, L. Xiao, F. Chen, Preparation and characterization of TiO₂
633 photocatalysts by Fe³⁺ doping together with Au deposition for the degradation of
634 organic pollutants, Appl. Catal. B: Environ. 88 (2009) 525-532.
- 635 [58] N. Kruse, S. Chenakin, XPS Characterization of Au/TiO₂ catalysts: binding energy
636 assessment and irradiation effects, Appl. Catal. A: Gen. 391 (2011) 367-376.
- 637 [59] V. Madhavi, P. Kondaiah, G. Mohan Rao, influence of silver nanoparticles on titanium
638 oxide and nitrogen doped titanium oxide thin films for sun light photocatalysis, Appl.
639 Surf. Sci. 436 (2018) 708-719.
- 640 [60] D. Sánchez-Rodríguez, M.G.M. Medrano, H. Remita, V. Escobar-Barrios,
641 Photocatalytic properties of BiOCl-TiO₂ composites for phenol photodegradation, J.
642 Environ. Chem. Eng. 6 (2018) 1601-1612.
- 643 [61] Y.-F. Zhu, J. Zhang, L. Xu, Y. Guo, X.-P. Wang, R.-G. Du, C.-J. Lin, Fabrication and
644 photoelectrochemical properties of ZnS/Au/TiO₂ nanotube array films, Phys. Chem.
645 Chem. Phys. 15 (2013) 4041-4048.
- 646 [59] Q. Sun, Y.-P. Peng, H. Chen, K.-L. Chang, Y.-N. Qiu, S.-W. Lai, Photoelectrochemical
647 oxidation of ibuprofen via Cu₂O-doped TiO₂ nanotube arrays, J. Hazard. Mater. 319
648 (2016) 121-129.

- 649 [63] J. Tian, H. Gao, H. Kong, P. Yang, W. Zhang, J. Chu, Influence of transition metal
650 doping on the structural, optical, and magnetic properties of TiO₂ films deposited on Si
651 substrates by a sol–gel process, *Nanoscale Res. Lett.* 8 (2013) 533.
- 652 [64] J. Singh, K. Sahu, A. Pandey, M. Kumar, T. Ghosh, B. Satpati, T. Som, S. Varma, D.K.
653 Avasthi, S. Mohapatra, Atom beam sputtered Ag-TiO₂ plasmonic nanocomposite thin
654 films for photocatalytic applications, *Appl. Surf. Sci.* 411 (2017) 347-354.
- 655 [65] Y. Zhang, C.X. Harris, P. Wallenmeyer, J. Murowchick, X. Chen, Asymmetric lattice
656 vibrational characteristics of rutile TiO₂ as revealed by laser power dependent Raman
657 spectroscopy. *J. Phys. Chem. C* 117 (2013) 24015-24022.
- 658 [66] K. Drogowska, Z. Tarnawski, A. Brudnik, E. Kusior, M. Sokołowski, K. Zakrzewska,
659 A. Reszka, N.T.H. Kim-Ngan, A.G. Balogh, RBS, XRR and optical reflectivity
660 measurements of Ti–TiO₂ thin films deposited by magnetron sputtering, *Mater. Res.*
661 *Bull.* 47 (2012) 296-301.
- 662 [67] E. Arcadipane, R. Sanz, M. Miritello, G. Impellizzeri, M.G. Grimaldi, V. Privitera, L.
663 Romano, TiO₂ Nanowires on Ti thin film for water purification, *Mater. Sci. Semicond.*
664 *Process.* 2016, 42 (2016) 24-27.
- 665 [68] E. Alves, N. Franco, N.P. Barradas, B. Nunes, J. Lopes, A. Cavaleiro, M. Torrell, L.
666 Cunha, F. Vaz, Structural and optical studies of Au doped titanium oxide films, *Nucl.*
667 *Instr. Meth. Phys. Res. B: Beam Interact. Mater. Atoms* 272 (2012) 61-65.
- 668 [69] A.M. Goodman, Optical interference method for the approximate determination of
669 refractive index and thickness of a transparent layer, *Appl. Opt.* 17 (1978), 2779-2787.
- 670 [70] J. Tauc, Optical Properties and Electronic Structure of Amorphous Semiconductors, in:
671 S. Mitra, (ed.), *Optical Properties of Solid*, Papers from the NATO Advanced Study
672 Institute on Optical Properties of Solids held August 7–20, 1966, at Freiburg, Germany,
673 Springer, Boston, USA, 1969.

- 674 [71] T.E. Tiwald, M. Schubert, Measurement of rutile TiO₂ dielectric tensor from 0.148 to 33
675 μm using generalized ellipsometry, *Proceedings of SPIE - The International Society for*
676 *Optical Engineering* 4103 (2000) 19-29.
- 677 [72] A. Wahl, K. Dawson, N. Sassi, A.J. Quinn, A. O’Riordan, Nanomolar trace metal
678 analysis of copper at gold microband arrays, *J. Phys. Conf. Ser.* 307 (2011) 01206.
- 679 [73] D. Li, X. Guo, H. Song, T. Sun, J. Wan, Preparation of RuO₂-TiO₂/nano-graphite
680 composite anode for electrochemical degradation of ceftriaxone sodium, *J. Hazard.*
681 *Mater.* 351 (2018) 250-259.
- 682 [74] M.V.B. Zanoni, J.J. Sene, H. Selcuk, M.A. Anderson, Photoelectrocatalytic production
683 of active chlorine on nanocrystalline titanium dioxide thin-film electrodes, *Environ. Sci.*
684 *Technol.* 38 (2004) 3203-3208.
- 685 [75] I. Sirés, J.A. Garrido, R.M. Rodríguez, P.L. Cabot, F. Centellas, C. Arias, E. Brillas,
686 Electrochemical degradation of paracetamol from water by catalytic action of Fe²⁺,
687 Cu²⁺, and UVA light on electrogenerated hydrogen peroxide, *J. Electrochem. Soc.* 153
688 (2006) D1-D9.
- 689 [76] E. Brillas, I. Sirés, C. Arias, P.L. Cabot, F. Centellas, R.M. Rodríguez, J.A. Garrido,
690 Mineralization of paracetamol in aqueous medium by anodic oxidation with a boron-
691 doped diamond electrode, *Chemosphere* 58 (2005) 399-406.
- 692 [77] L.C. Almeida, S. Garcia-Segura, N. Bocchi, E. Brillas, Solar photoelectro-Fenton
693 degradation of paracetamol using a flow plant with a Pt/air-diffusion cell coupled with a
694 compound parabolic collector: Process optimization by response surface methodology,
695 *Appl. Catal. B: Environ.* 103 (2011) 21-30.
- 696

697 **Figure captions**

698 **Fig. 1.** General XPS spectrum of the TiO₂/Au/TiO₂ multilayer thin film.

699 **Fig. 2.** Raman spectrum of the TiO₂/Au/TiO₂ multilayer thin film.

700 **Fig. 3.** EFA characterization of (A) TiO₂/Au/TiO₂ multilayer thin film, (B) Ti⁴⁺, and (C) Au.

701 **Fig. 4.** (A) Transmittance spectrum of the TiO₂ thin film and TiO₂/Au/TiO₂ multilayer thin
702 film. (B) Tauc plot for the determination of the band gap of the undoped and doped films.

703 **Fig. 5.** (A) Qualitative comparison of the photoluminescence emission spectra of the
704 TiO₂/Au/TiO₂ film (blue curve) and a TiO₂ blank (red curve) from 3.6 to 2.0 eV. (B) Detailed
705 photoluminescence emission spectrum of the same TiO₂/Au/TiO₂ multilayer thin film.

706 **Fig. 6.** Cyclic voltammograms of (A) pure gold, (B) undoped TiO₂ thin film, and (C)
707 TiO₂/Au/TiO₂ multilayer thin film, all of 1 cm² geometric area, in 0.050 M N₂SO₄ at pH 3.0.
708 The cell contained a Pt cathode and Ag|AgCl (3 M KCl) as reference electrode. Scan rate 100
709 mV s⁻¹.

710 **Fig. 7.** Normalized paracetamol concentration decay vs. electrolysis time for the (A) EO in
711 0.050 M Na₂SO₄, (B) PEC in 0.050 M Na₂SO₄, and (C) PEC in 0.035 M Na₂SO₄ + 0.015 M
712 NaCl treatments of 100 mL of solutions with different drug concentrations at pH 3.0 using a
713 three-electrode cell with a TiO₂/Au/TiO₂ multilayer thin-film anode and a stainless steel
714 cathode at $I_{app} = 0.50$ mA. The PEC trials were performed with irradiation from a 36-W LED
715 UVA lamp.

716 **Fig. 8.** Change of normalized paracetamol concentration with electrolysis time for the PEC +
717 PEF treatment of 100 mL of 39 mg L⁻¹ of drug in 0.035 M Na₂SO₄ + 0.015 M NaCl and 0.50
718 mM Fe²⁺ at pH 3.0 using a three-electrode cell containing a TiO₂/Au/TiO₂ multilayer thin-
719 film anode and an air-diffusion cathode, at $E_{an} = +4.0$ V vs Ag|AgCl (3 M KCl), with
720 irradiation from a 36-W LED UVA lamp.

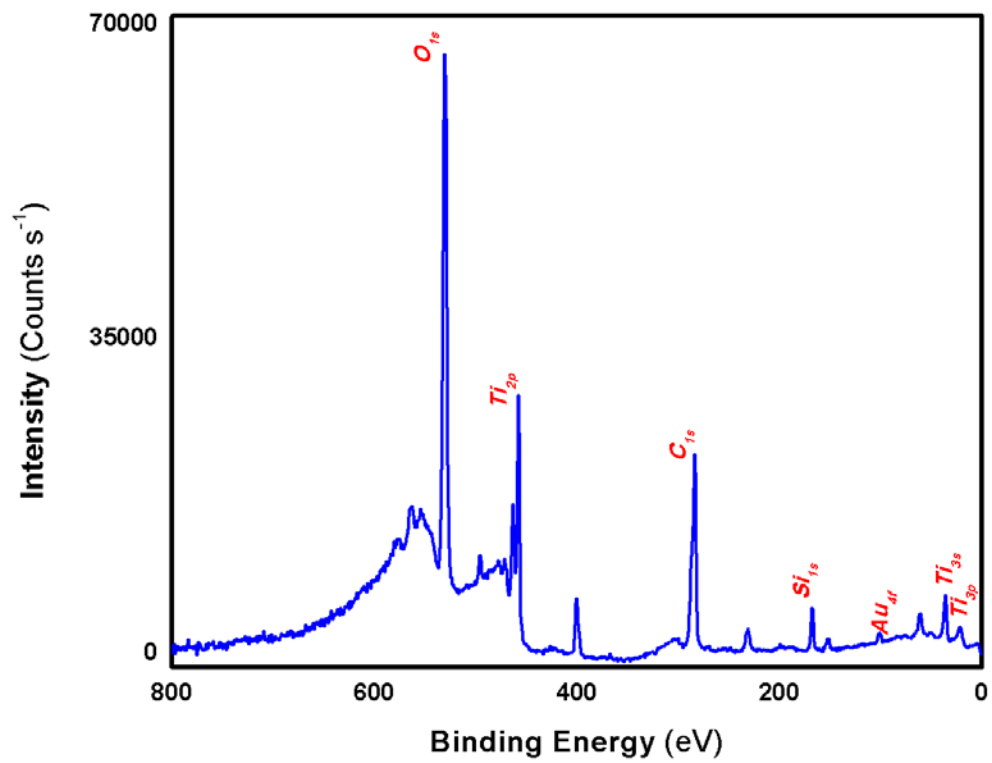


Fig. 1

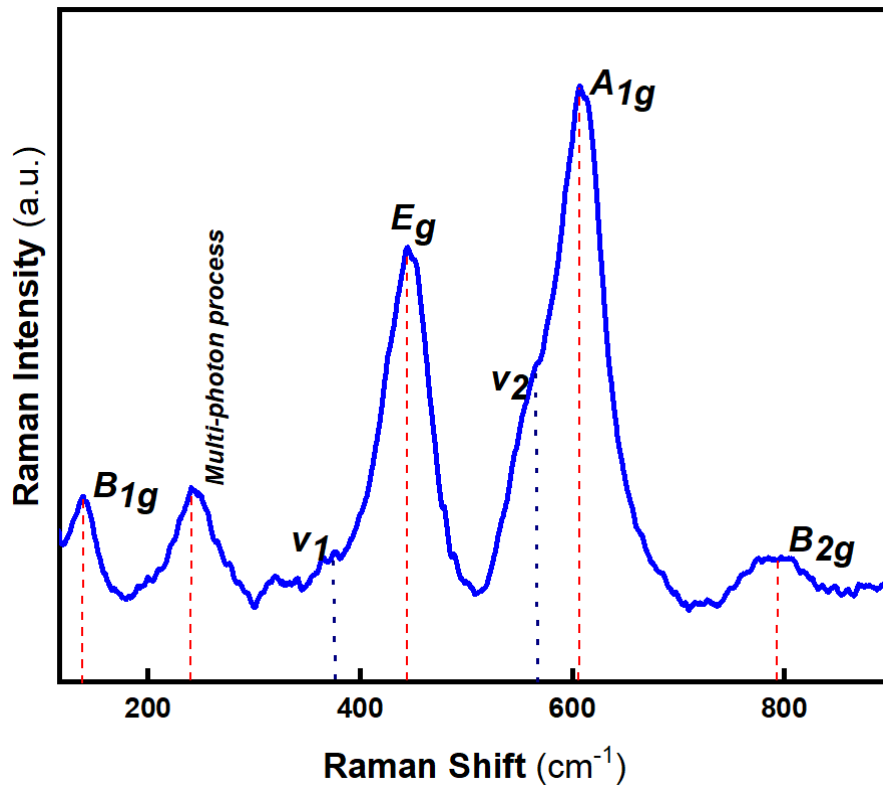


Fig. 2

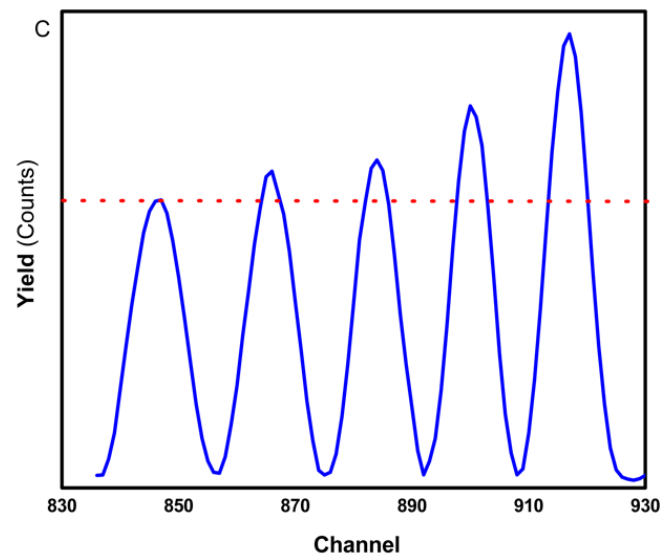
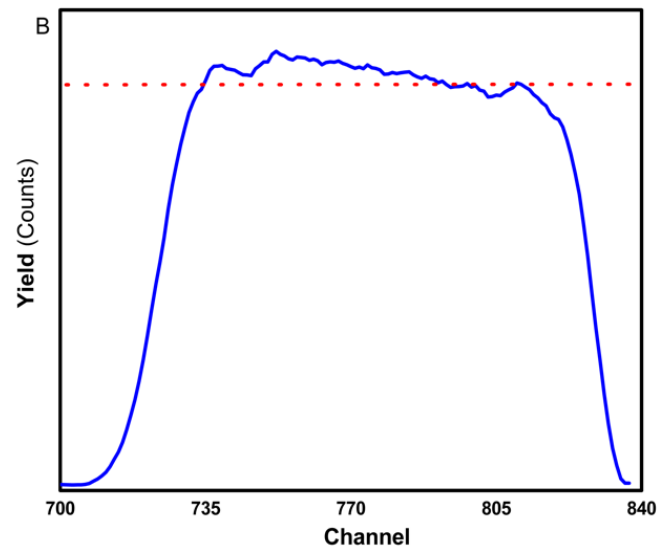
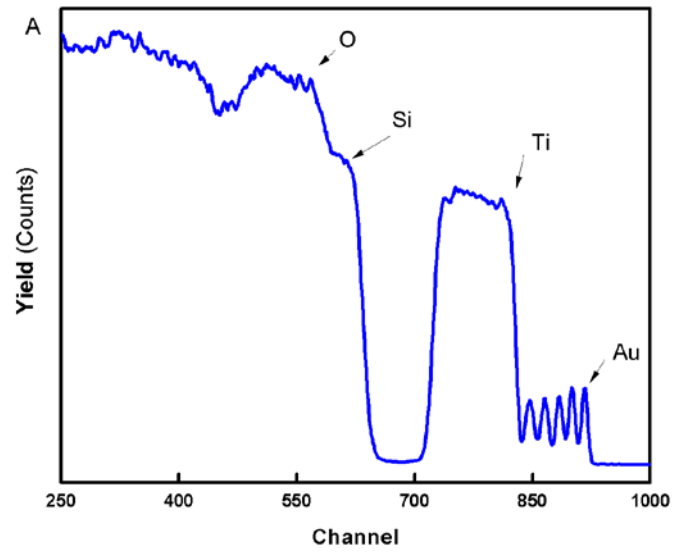


Fig. 3

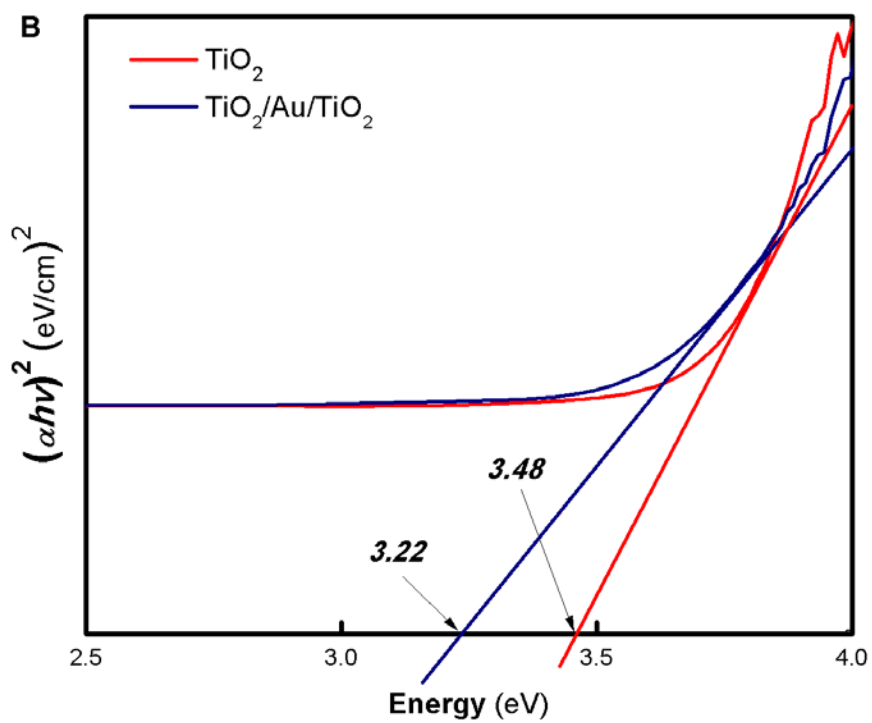
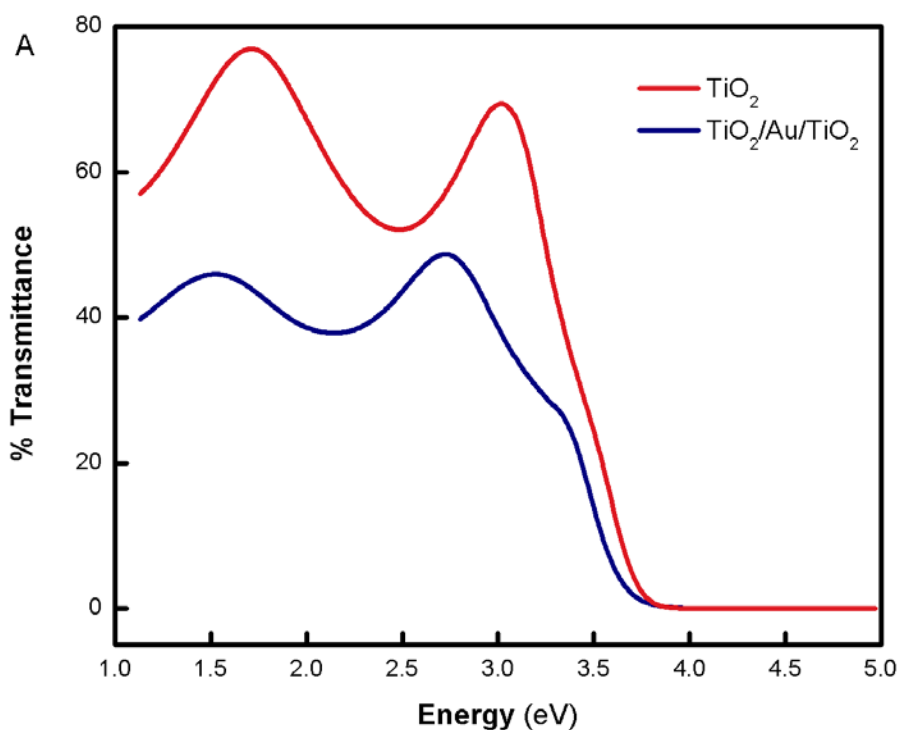


Fig. 4

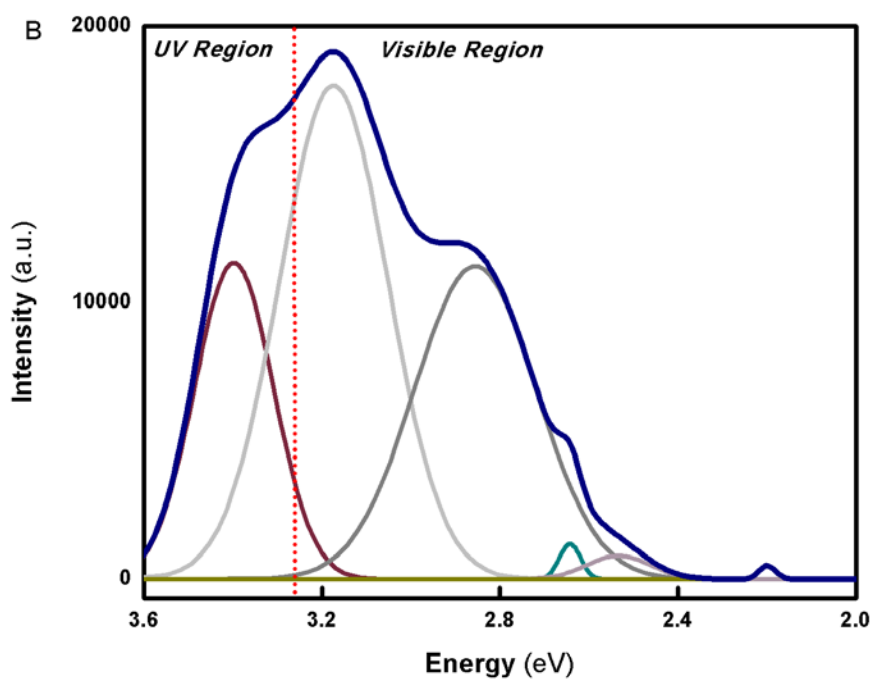
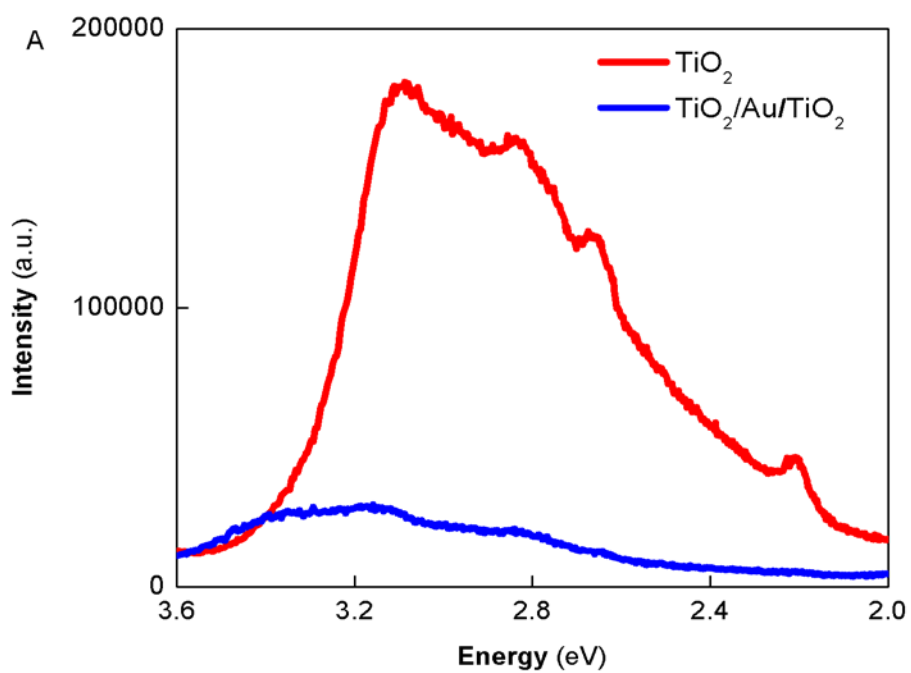


Fig. 5

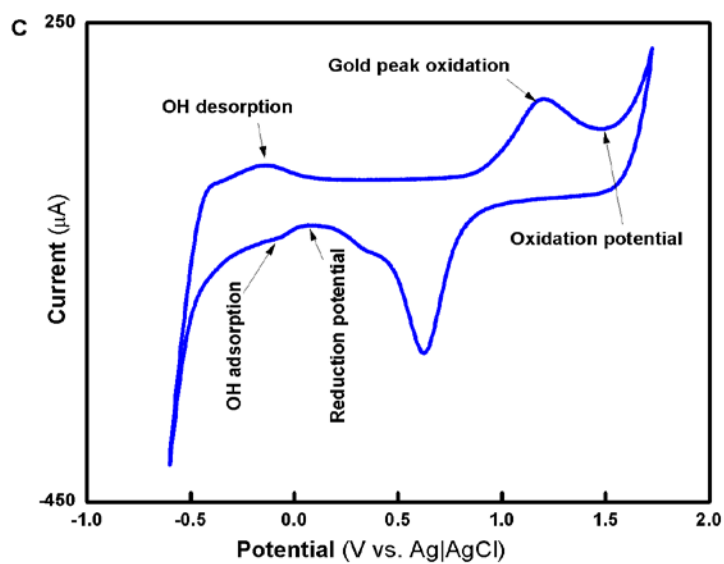
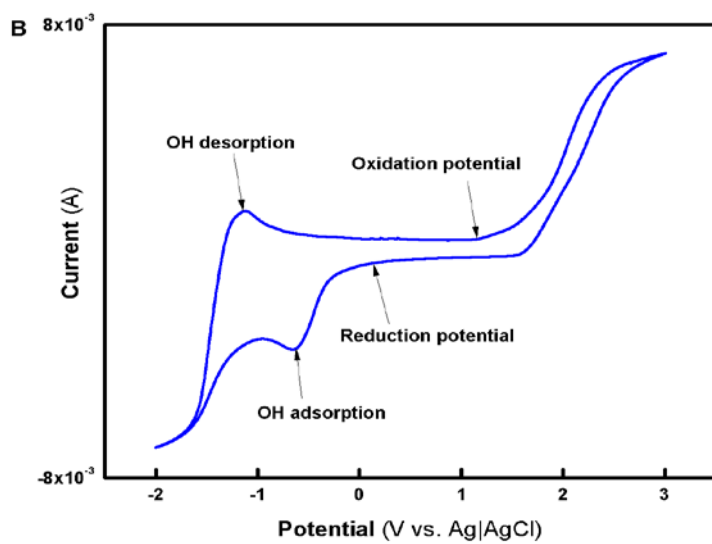
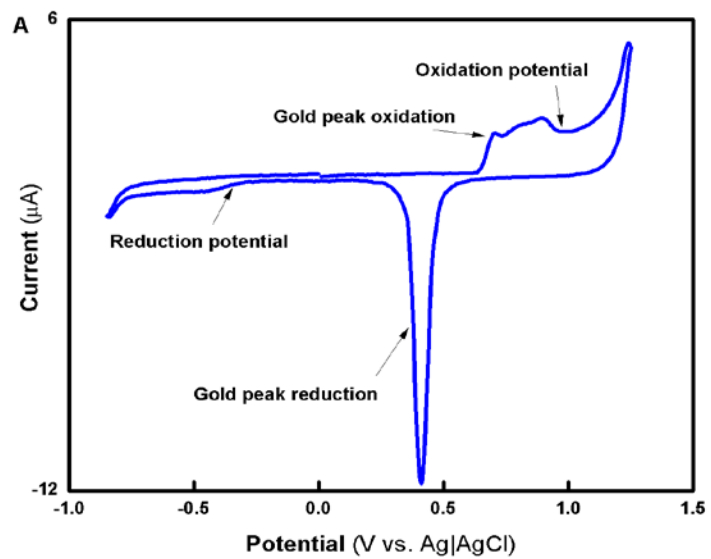


Fig. 6

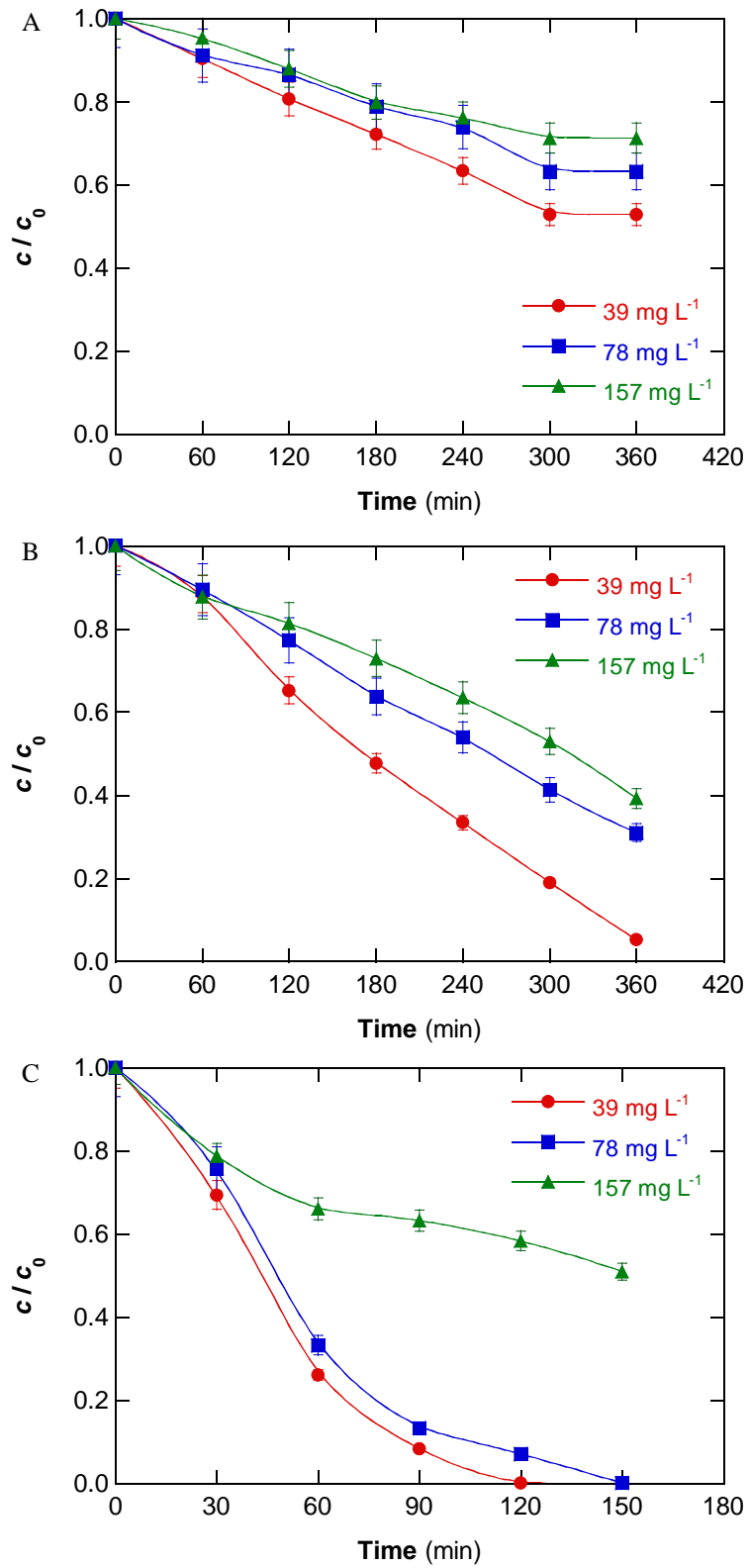


Fig. 7

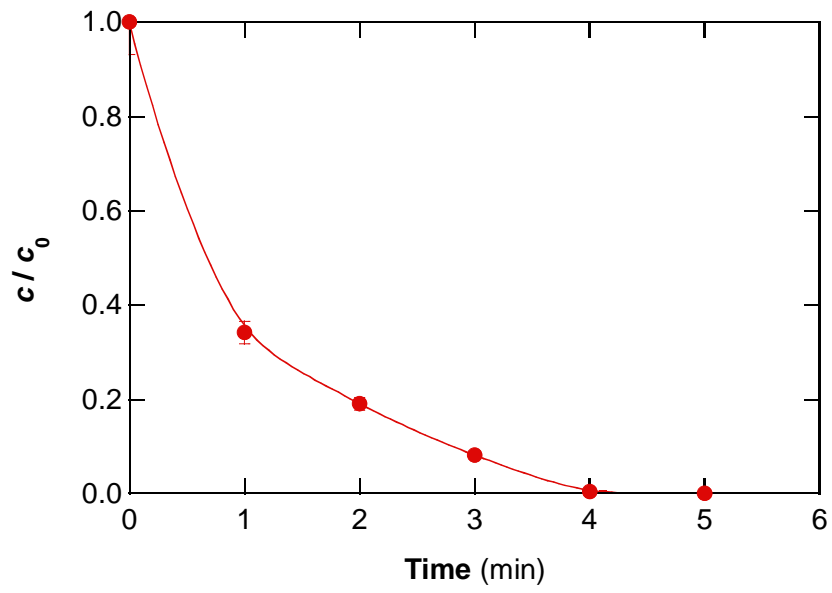


Fig. 8